


Nanofiltration membranes with ultra-high negative charge density for enhanced anion sieving and removal of organic micropollutants

Received: 12 June 2024

Accepted: 2 April 2025

Published online: 8 May 2025

 Check for updates

Xiaoming Xu^{1,2}, Yuxuan Chen¹, Zhiwei Wang¹, Guoyan Hua¹, Zepeng Zhang¹, Shengnan Liu¹, Pengrui Jin^{2,3}, Fuqiang Liu¹✉ & Huanting Wang²✉

Nanofiltration membranes with high charge density are highly attractive for selectively removing organic micropollutants and divalent anions from water environments. Here we constructed polyamide (PA) membranes with ultra-high negative charge density via a sea-squirt nanofibrillated cellulose restricted interfacial polymerization process. Sea-squirt nanofibrillated cellulose, which contains a high content of 7.0% carboxyl groups and 29.8% hydroxyl groups, effectively fettered piperazine and regulated the interfacial polymerization reaction kinetics. As a result, the optimized membrane had an ultra-high zeta potential of -148 mV at pH 7 and a charge density of -32.6 mC m⁻². This membrane achieved outstanding performance metrics, including a water permeance of 41.5 l m⁻² h⁻¹ bar⁻¹, exceptional SO₄²⁻/Cl⁻ selectivity of 144.5 and greatly increased water/organic micropollutant selectivity. Molecular dynamics simulations revealed a 73.1% reduction in the diffusion rate of piperazine due to competitive forces, leading to a PA surface enriched with -COOH groups. This work provides an effective strategy for tuning the PA membrane charge density to increase water purification and wastewater treatment efficiency.

Extending the water supply from seawater, sewage and brackish water is critical for tackling the global water scarcity challenge¹. Moreover, organic micropollutants (OMPs), such as endocrine disrupting compounds², antibiotics³ and pharmaceutically active compounds⁴, have been widely detected in complex water environments, posing great threats to ecological security. Nanofiltration (NF)-based water treatment technologies serve as a vital system for guarding recycled water security and increasing freshwater supplies and are promising for ion sieving and micropollutant removal^{5–7}. In typical NF membrane synthesis, interfacial polymerization (IP) of monomeric piperazine (PIP) and trimesoyl chloride (TMC) in two immiscible phases are used

to form a polyamide (PA) active layer^{8,9}. However, the millisecond polycondensation reaction makes tuning the nanostructure challenging. As a result, NF membranes are subjected to an inherent trade-off between permeability and solute selectivity¹⁰.

Recently, diverse efforts have been devoted to overcoming the trade-off limitation by improving the pore structural uniformity^{11–13}, reducing the thickness^{14–16} and increasing the permeation area^{17–19}. Nevertheless, precise control over charge density—a critical parameter governing nanofluidic transport in NF models—remains challenging due to the heterogeneous distribution of amine and carboxyl groups on PA surfaces. A notable advancement emerged through hexagonal polytype

¹State Key Laboratory of Water Pollution Control and Green Resource Recycling, School of the Environment, Nanjing University, Nanjing, China.

²Department of Chemical and Biological Engineering, Monash University, Clayton, Victoria, Australia. ³Department of Chemical Engineering, KU Leuven, Leuven, Belgium. ✉e-mail: lfq@nju.edu.cn; huanting.wang@monash.edu

(I_h) ice-confined IP strategy to form highly ionized PA membranes by increasing the membrane area²⁰. Whereas alternative approaches such as incorporating charged nanomaterials into PA matrices have also been proposed²¹, their effectiveness has been limited. To date, the reported charge density of PA membranes ranges from -1 to -10 mC m⁻² when calculated using the Gouy–Chapman equation²². When the charge density ionized from carboxyl groups increases, the co-ion distribution in the feed solution increases, and the transmembrane energy barrier of anions at the interface increases through induced polarized charges²³. Therefore, anion sieving and negatively charged OMPs can be markedly improved.

The regulation of the IP process is the most pivotal step in controlling charge density²⁴. Researchers have confirmed that active sites on exogenous additives can adjust the transmission rate of diamines during IP²⁵. The PA structure is formed through a diffusion-limited reaction, and amide linkages can be regulated by the migrating diffusion of amine monomers to the reaction zone¹³. Owing to the erratic physico-chemical resistance from the boundary interface to the reaction zone, the diffusion rate and flux of the amine monomers in the water phase undulate, resulting in a heterogeneous reaction. Oxygen-dominated groups (named [O] groups, such as carboxyl and hydroxyl groups) can interact with amine groups through electrostatic attraction^{11,22} and hydrogen bonding²² due to the high electronegativity of the oxygen atom. We assumed that the regulatory behaviour may lead aqueous monomers to distribute uniformly at the interface and form a homogeneous incipient layer. The oriented thin layer prevents PIP from crossing the incipient layer and constructing a low-cross-linked/acyl chloride monomer terminal structure on the front PA surface. Eventually, the carboxy-rich functional group (R-COOH/R-COO⁻) produced by acyl chloride hydrolysis generates a high charge density.

On the basis of the assumption discussed above, we preassembled sea-squirt nanofibrillated cellulose (SNFC) to form a uniform interlayer and then through restricted IP (RIP) to yield highly ionized PA membranes (Fig. 1a). NFC, derived from biomass, is valued for its oxygen-rich groups and high aspect ratio (length/diameter > 10,000), providing controllable surface chemistry, strong mechanical properties and flexible assembly methods^{26,27}. Therefore, NFC has the potential to effectively control aqueous monomers, facilitating slow diffusion and restricted spatial distribution, allowing precise regulation of the PA layer. Comprehensive physico-chemical characterization and separation experiments were conducted to verify the exact control of the surface charge density and efficient sieving of target substances. Molecular dynamics (MD) simulations revealed how SNFC affected PIP diffusion via competitive effects to construct highly ionized membranes.

Physico-chemical properties of PA–SNFC membranes

Three kinds of biomass, bacterial cellulose (BC), wood NFC (WNFC) and SNFC, and three different extraction methods, ultrasonication, acid hydrolysis and modified 2,2,6,6-tetramethylpiperidinoxy (TEMPO) oxidation, were compared to obtain the NFCs with the highest [O] group exposure density (Supplementary Figs. 1–4). The 1D SNFC extracted from sea squirts by the modified TEMPO oxidation method presented the highest O content of 48.6% (including 7.0% -COOH and 29.8% -OH), while exhibiting high dispersion, a high aspect ratio, excellent robustness and a tertiary crystal structure (Supplementary Figs. 5–8). After vacuum self-assembly, the uniform SNFC layer presented an extremely hydrophilic surface with a water contact angle of 20.7° (Supplementary Figs. 9 and 10). The weak thin film interference phenomenon indicated the structural continuity of the SNFC layer (Supplementary Fig. 11). Additionally, the pore size of the SNFC interlayer reached 12.6 nm (Supplementary Fig. 12), which was greatly smaller than the 0.22 μm pore size of the polyether sulfone (PES) substrate.

The refined PA layer was fabricated via the SNFC–RIP process on the SNFC/PES composite substrate and named the PA–SNFC

membranes (Supplementary Fig. 13). The chemical composition and charge properties of the PA surface were investigated in detail. X-ray photoelectron spectroscopy (XPS) revealed that the O 1s content increased from 16.4% to 18.7% (Supplementary Table 1). Moreover, the O 1s high-resolution spectra (Fig. 1b and Supplementary Fig. 14) revealed that the O=C–O bond (correlated with -COOH) increased from 32.9% to 45.7%, highlighting the considerable ability of SNFC to tune the chemical composition. Similarly, the C 1s high-resolution spectra, N 1s high-resolution spectra and core chemical bond contents also revealed the reduced free amino groups and increased free carboxyl groups (Supplementary Figs. 15 and 16 and Supplementary Table 2). The cross-linking degree of PA–SNFC membranes decreased gradually, indicating a porous membrane structure (Supplementary Table 1).

With a higher -COOH content than that reported for PA NF membranes, the negative charge density and ionization degree of the membrane are expected to be increased. Kelvin probe force microscopy (KPFM) potential scan results (Fig. 1c) revealed an ionized gap after the -COOH content increased, and the surface potential increased by -189 mV (arithmetic mean; Supplementary Fig. 17). Although the surface potential distributions of the PA–WNFC membrane and PA–BC membrane were strengthened (Supplementary Fig. 18), they still cannot reach the ideal level of the PA–SNFC membrane. Furthermore, the zeta potential (Fig. 1d) along the shear plane of the PA–SNFC membranes decreased gradually and reached -148 mV at pH 7. The remarkable zeta potential indicated that the membrane surface carried a substantial negative charge and exhibited a highly ionized state in aqueous solution. According to the Gouy–Chapman equation, the charge density for PA–SNFC was calculated to be -32.6 mC m⁻² (Fig. 1e), which is three times greater than that reported in the literature^{28,29}. In addition, the increase of polar -COOH groups favoured membrane hydrophilicity, as shown in Supplementary Fig. 19. This improvement in hydrophilicity could reduce water flow resistance and minimize the adsorption of hydrophobic contaminants³⁰.

The surface morphology and pore structure of the PA–SNFC membrane are presented in Fig. 2. The SNFC interlayer made up for the defects of the substrate, and the PA layer imprinted a filamentous morphology of SNFC networks (Fig. 2a–c). Without the SNFC interlayer, the macroporous substrate could not form or support the consecutive polyamide layer (Supplementary Fig. 20). Atomic force microscopy (AFM) images (Fig. 2d,e) confirmed that a smooth PA layer formed above the SNFC interlayer. The average roughness (R_a) decreased from 91.7 nm to 26.9 nm during the densification of the SNFC interlayer (Supplementary Fig. 21). As shown in Supplementary Fig. 22, owing to the high compatibility between the PA layer and SNFC interlayer, the two layers tightly integrated and covered the PES substrate. The transmission electron microscopy (TEM) of the resin section shown in Fig. 2f and Supplementary Fig. 23 revealed that the thickness of the SNFC interlayer increased sequentially by approximately 10 nm, whereas the thickness of the PA layer decreased from 18.4 ± 0.4 nm to 14.0 ± 1.3 nm. The XPS spectrum revealed that as the number of defects in the PA layer decreased, the S 2p peak gradually disappeared (Supplementary Fig. 24).

Nanoindentation tests (Supplementary Figs. 25 and 26a,b) revealed that the highly ionized membrane had a hardness of up to 63.2 MPa and an elastic modulus of 460 MPa, confirming the high mechanical stability of the membrane. In addition, the scratch test (Supplementary Fig. 26c,d) demonstrated that the PES substrate and SNFC interlayer of the highly ionized membrane have strong interfacial adhesion, with the critical load at the peeled onset reaching 32.0 μN.

The more uniform pore size distribution of PA–SNFC membranes was confirmed through both the pore size distribution simulated by neutral molecules and positron annihilation lifetime spectroscopy (PALS). The molecular weight cut-off (MWCO) was determined by the rejection of 200 mg l⁻¹ polyethylene glycol (PEG) with different molecular weights, as shown in Fig. 2g. The MWCO decreased from 996 Da to

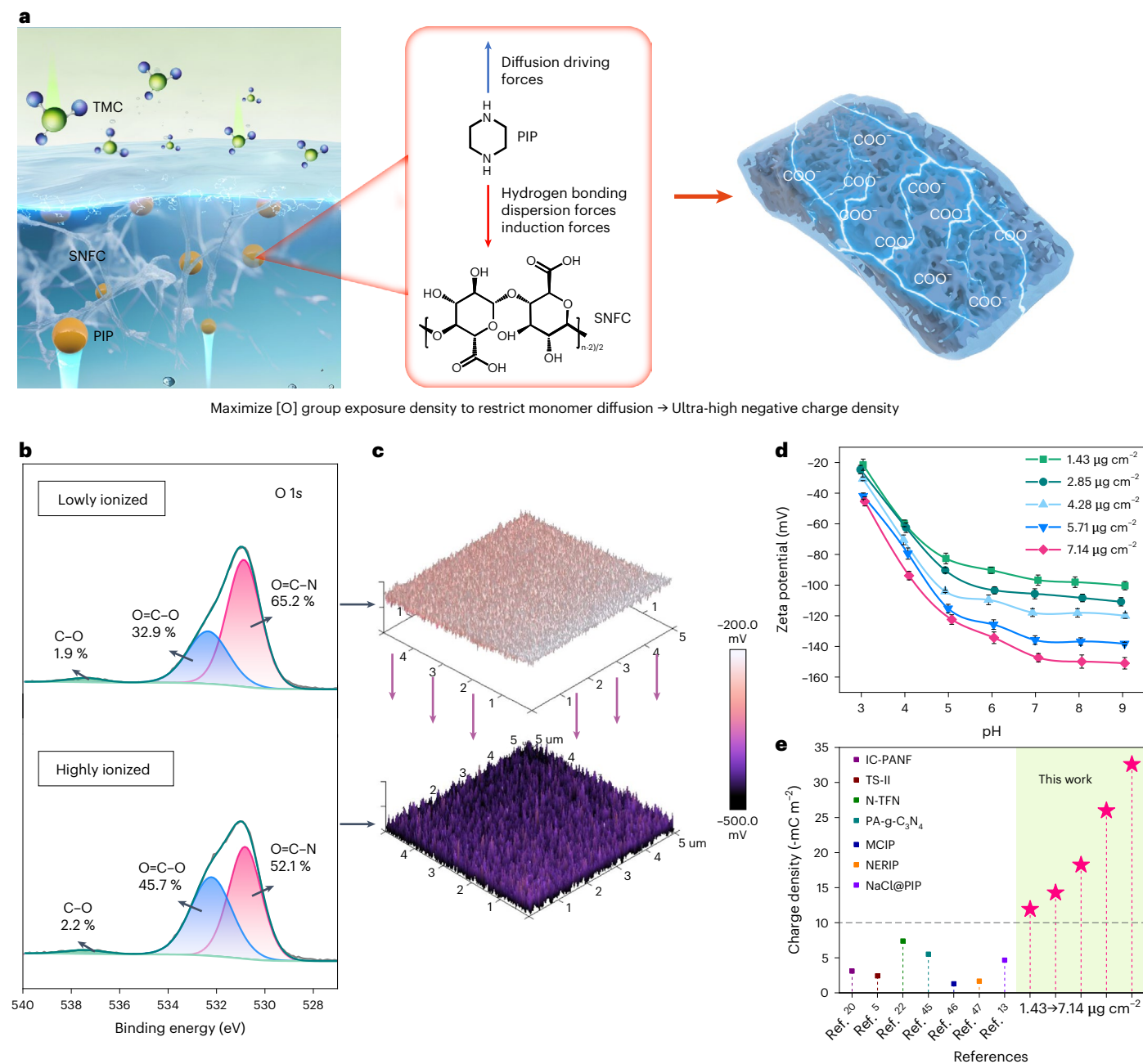


Fig. 1 | Regulation and highly ionized characteristics of PA-SNFC membranes.

a, Schematic illustration of highly ionized membranes prepared by the SNFC-RIP process. **b, c**, XPS O 1s high-resolution spectra (**b**) and corresponding KPFM images of the lowly ionized membrane (fewest SNFC dosage of $1.43 \mu\text{g cm}^{-2}$) and highly ionized membrane (highest SNFC dosage of $7.14 \mu\text{g cm}^{-2}$) (**c**). **d**, Zeta potential of PA-SNFC membranes with different SNFC dosages. Error

bars represent the standard deviation (s.d., $n = 3$, n derived from different experimental units) and data are presented as mean values \pm s.d.

e, Comparison of the charge densities of PA-SNFC and other state-of-the-art membranes^{5,13,20,22,45-47}. The green shading represents PA-SNFC membranes with different SNFC dosages.

475 Da, indicating that the PA-SNFC membranes transitioned from a loose structure to a denser one^{31,32}. The probability density function (Fig. 2h) was fitted mathematically by the Stokes radius⁶. The membrane pore size exhibited two trends due to SNFC: the peak shifted towards smaller pore sizes and the half-width narrowed. According to Supplementary Table 3, the average pore diameter (μ_p) decreased from 1.02 nm to 0.58 nm. By monitoring the positron annihilation time via PALS (Fig. 2i and Supplementary Fig. 27), the probability density functions were also identified as having a smaller and more uniform free volume distribution³³. Presumably, this was the result of strengthened regulation with increasing [O] content (Supplementary Fig. 28). RIP reactions yielded PA layers with narrower distributions of free volume,

whereas less regulated reactions resulted in membranes with broader distributions, featuring heterogeneous free volume pores.

The PA structure originated from the transient polymerization of small polymer clusters and then cluster-cluster aggregation formed a solid core of the polymer membrane with a certain thickness, which evolved into an incipient membrane and controlled the transmembrane diffusion of amine monomers^{12,34}. The integrity of the incipient membrane is correlated with the final PA nanostructure³⁵. According to the Frege kinetic model, PIP diffuses slowly and steadily to form a thin and uniform incipient layer, thereby further preventing the transmembrane movement of PIP from reacting with TMC in the organic phase³⁶. It is crucial to explore the reactions and diffusion of monomers at the interface.

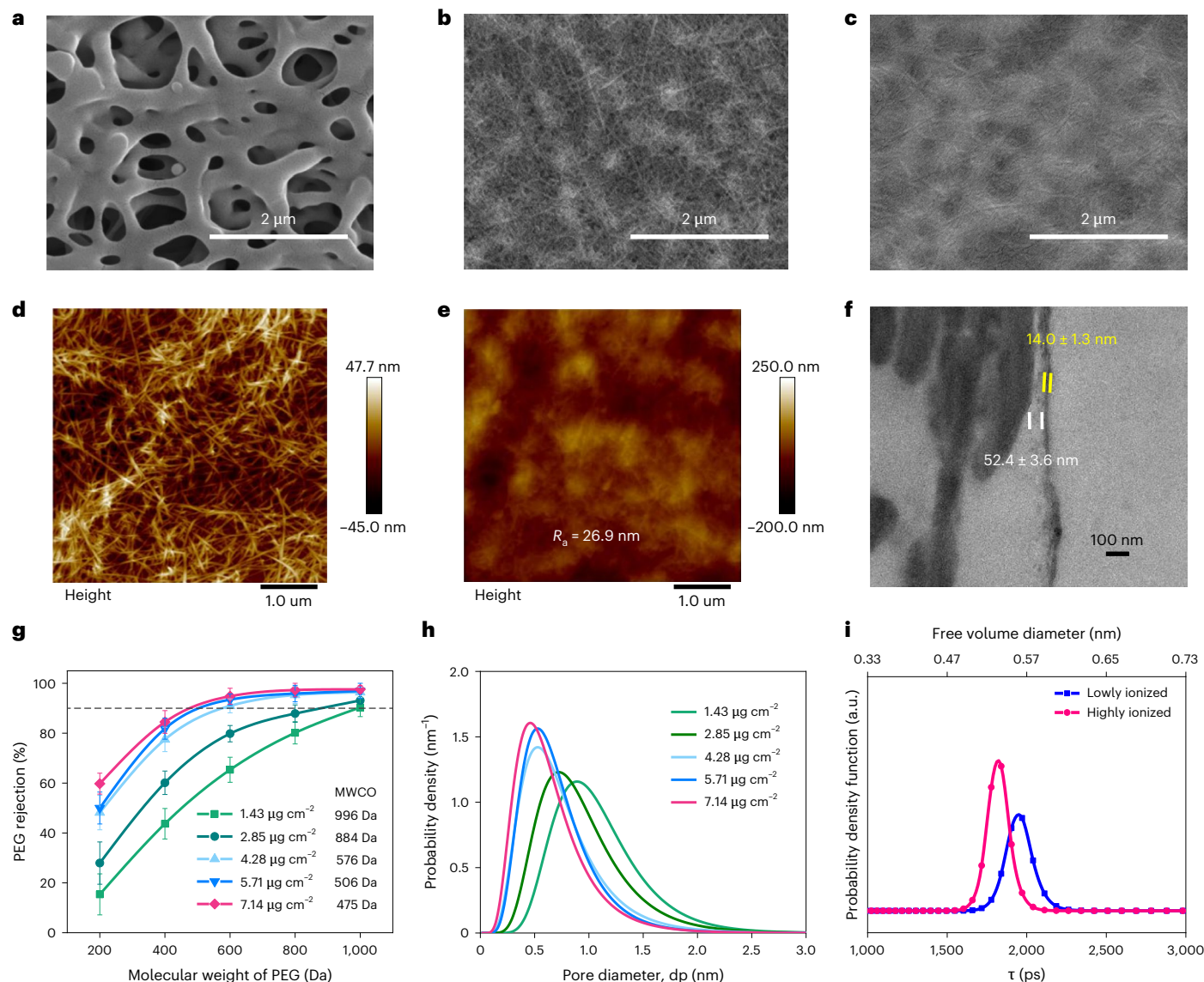


Fig. 2 | Physico-chemical structure of PA-SNFC. **a–c**, Scanning electron microscopy (SEM) images of PES macropore substrate (**a**), SNFC/PES composite substrate (**b**) and PA-SNFC membrane (**c**). **d, e**, AFM images of the SNFC interlayer (**d**) and PA-SNFC surface (**e**). **f**, TEM cross-sectional image of PA-SNFC membrane. ImageJ software was used to measure the thickness of the PA layer

(yellow font) and SNFC interlayer (white font). **g**, PEG rejection curves. **h**, Pore size distribution curves. **dp**, pore diameter. **i**, Probability density function of the PALS of the PA-SNFC membranes. Error bars in **g** represent the standard deviation (s.d., $n = 3$, n derived from different experimental units) and data are presented as mean values \pm s.d.

MD simulation of the SNFC-RIP process

By means of MD simulations, we investigated the diffusion behaviour of amine monomers from the intrinsic phase to the boundary interface in the presence of SNFC and how the affected PIP diffusion restricted the free and boundary-free IP reactions to achieve the construction of an ultra-negatively charged surface. As shown in Fig. 3a and Supplementary Fig. 29, an *n*-hexane phase (left) and a water phase (right) with/without SNFC were constructed. In the initial state, PIP was dispersed uniformly in the water phase. As the reaction progressed, PIP tended to move towards the water-organic interface under the diffusion driving force. However, owing to the high concentration of active [O] sites exposed to SNFC, PIP was affected by SNFC-PIP intermolecular forces such as hydrogen bonding, the induction force and the dispersion force. When the simulation terminated, PIP diffusion in the presence of SNFC was notably lower than that in the pure PIP model.

Figure 3b showed the number density of each substance along the *z* axis at the final state. The water/*n*-hexane interface of the two models was at -44 \AA , depending on the distribution of water and

n-hexane molecules. Compared with that of the PIP model, the peak area of PIP in the PIP-SNFC model was reduced at the interface. According to Supplementary Fig. 30, SNFC was more likely to remain in the water phase because the van der Waals force between SNFC and water ($-658.6 \text{ kJ mol}^{-1}$) was much stronger than that between SNFC and *n*-hexane ($-46.7 \text{ kJ mol}^{-1}$). The PIP diffusion coefficient (*D*) can be measured via Einstein's relationship on the basis of the slope of the MSD curve. As depicted in Fig. 3c, the *D* of the PIP-SNFC model was $1.07 \times 10^{-5} \text{ cm}^2 \text{ s}^{-1}$, which was 73.1% lower than that of the PIP model ($3.97 \times 10^{-5} \text{ cm}^2 \text{ s}^{-1}$). The radial distribution function of one representative oxygen atom in the regulator SNFC around different atoms in PIP and water at the initial and final states offered further insights (Fig. 3d). Commencing from a random state, the peak strength of SNFC (O)-H₂O (H) weakened and that of SNFC (O)-PIP (N) increased, indicating that PIP partially replaced H₂O and tightly surrounded SNFC as the simulation progressed. Ending an equilibrium state, the differential *g*(*r*) distribution along with the distance of SNFC (O)-PIP (N) confirmed their interaction force.

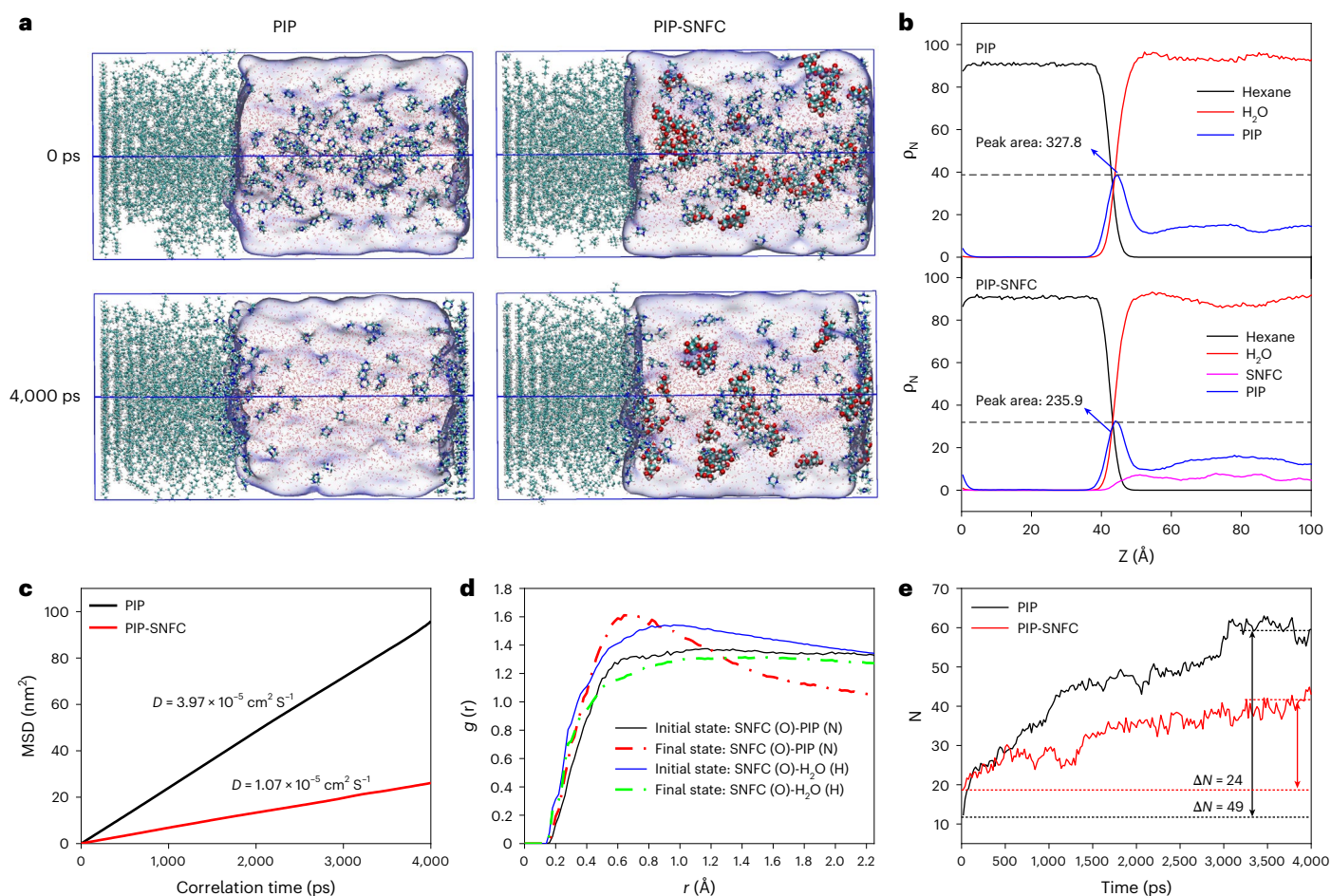


Fig. 3 | MD simulation of the SNFC-RIP process. **a**, Snapshots of models at the initial state and final state: the left chamber contains hexane, and the right chamber contains water, PIP molecules and with/without SNFC. **b**, The number density of *n*-hexane, H₂O, SNFC and PIP along the *z* axis in the PIP model and PIP-SNFC model at the final state. **c**, Time dependence of the mean square

displacement (MSD) curves of PIP molecules in the PIP model and PIP-SNFC model. **d**, Radial distribution function ($g(r)$) of O atoms in SNFC around PIP (N) and water (H) in the PIP-SNFC model at the initial state and final state. **e**, The variation in the number of PIP molecules compared with the initial value (N_0).

The variation in the number ($\Delta N = N - N_0$; Fig. 3e) of interfacial PIP molecules revealed that the ΔN of PIP with SNFC (~ 24) was 52% lower than that without SNFC (~ 49). Supplementary Fig. 31 shows the quantified number of hydrogen bonds in the initial and final states. Beginning with 24 between SNFC and the PIP monomer, the number increased to 40 when diffusion reached equilibrium. The increased number of hydrogen bonds together with the induction force and dispersion force acting on PIP induced a decrease in its diffusion rate and formed a thin incipient PA layer. Moreover, the diffusion rate of PIP under actual conditions was measured via a UV spectrophotometer (Supplementary Fig. 32). In the detection range, the PIP diffusion of the PIP-SNFC model was slower and gentler than that of the PIP model, which confirmed the conclusion of the MD simulation.

To explore the reaction kinetics of the RIP process, two groups of PA-SNFC membranes formed at the free water/organic interface were explored (Supplementary Fig. 33). Generally, the kinetics of the IP reaction are controlled by the diffusion rate of the monomers, the reactivity at the interface and the rate of membrane growth. At unrestricted concentrations and in free space, the reactivity between PIP and TMC remains constant. However, when the concentration of amine monomers at the interface decreased, the reaction rate was limited accordingly. The lower mass transfer and reaction rates result in less heat being released¹⁶ during the RIP reaction (Group A) than during the unrestricted IP reaction (Group B). Therefore, the lower heat generation prevented a sharp rise in local temperature, minimizing the

interfacial instability caused by Rayleigh-Bénard convection¹⁴ and bubbles formation³⁷ (Supplementary Fig. 34a). However, the accumulation of heat and HCl in Group B led to the formation of micron-sized bubbles (Supplementary Fig. 34b).

After the aggregation of the polymer clusters, the convection-driven self-healing effect led to the formation of a continuous incipient layer. Owing to the uniformity of the continuous layer, the upward penetration of PIP was blocked, thus forming a TMC-rich/TMC-terminated linear cross-linked structure on the front surface of the PA. As depicted in Supplementary Fig. 34c, the O content at 0 nm reached 18.3%. In contrast, the non-uniform PA membrane in Supplementary Fig. 34d had an oxygen content of only 15.8% at 0 nm. At 10 nm, both membranes had a fully cross-linked PA structure, where carbon from the polymer backbone became dominant. Beyond 20 nm, Group A's membrane transitioned into a PIP-rich/PIP-terminated linear cross-linked structure and began to interlace with the SNFC layer (Supplementary Fig. 35), and the oxygen content gradually increased thereafter. In Group B, this transition into the PA and SNFC interface only occurred at 60 nm, and the SNFC layer continued to extend up to 100 nm. For Group A, a sulfur content of 1.4% was detected at 100 nm, indicating the appearance of the PES substrate.

Fast permeation and precise anion sieving

High permeability and precise ion sieving are crucial for accessing next-generation membranes. Na₂SO₄ and NaCl were selected as model

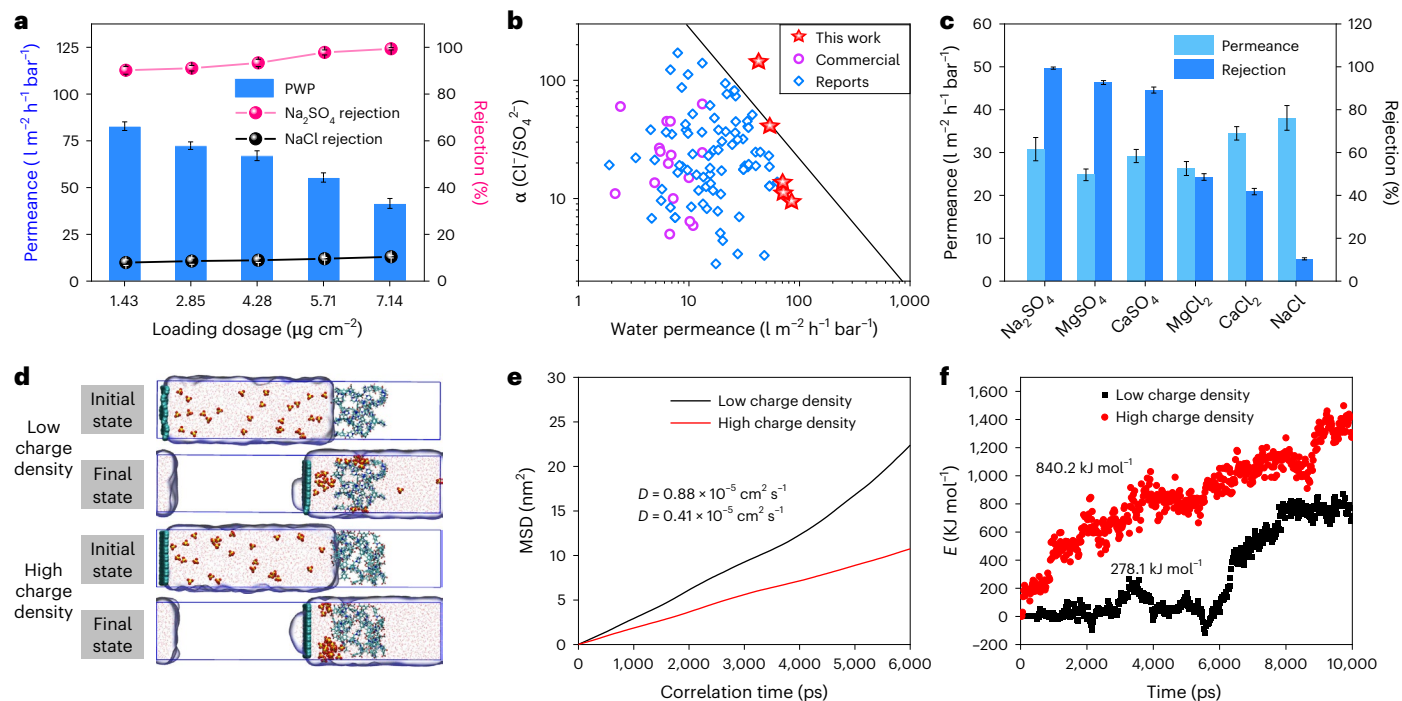


Fig. 4 | Ion sieving performance and transmembrane behaviour according to MD simulations. **a**, PWP, Na_2SO_4 rejection and NaCl rejection of PA-SNFC membranes. The salt concentration was 1 g l^{-1} ; the applied pressure was 4 bar; the effective membrane area was 7.07 cm^2 ; and the temperature was 298 K. **b**, Performance comparison of mono-/bivalent anion selectivity and water permeance with those of commercial and state-of-the-art membranes. The details are presented in Supplementary Table 4. **c**, Permeance and rejection of Na_2SO_4 , MgSO_4 , CaSO_4 , MgCl_2 , CaCl_2 and NaCl by PA-SNFC with an SNFC dosage of $7.14 \mu\text{g cm}^{-2}$. Error bars in **a** and **c** represent the standard deviation (s.d., $n = 3$,

n derived from different experimental units) and data are presented as mean values \pm s.d. **d**, Snapshots of MD simulations of the low charge density membrane model and high charge density membrane model at the initial and final states: the left chamber contained SO_4^{2-} and water, and the right chamber contained PA structures with different charge densities. **e**, Time dependence of the MSD curves of SO_4^{2-} for the low ionization intensity model and high ionization intensity model. **f**, Coulomb repulsive forces between SO_4^{2-} and carboxyl groups in the PA structure of the low ionization intensity model and high ionization intensity model.

solutes to assess the ion sieving potential of PA-SNFC. As optimized in Supplementary Fig. 36, 0.05 w/v% PIP and 0.04 w/v% TMC were selected for subsequent reactions. Figure 4a and Supplementary Fig. 37 show that the pure water permeance (PWP) reached $41.5 \text{ l m}^{-2} \text{ h}^{-1} \text{ bar}^{-1}$ when the SNFC dosage was $7.14 \mu\text{g cm}^{-2}$ and that the Na_2SO_4 solution permeance reached $30.8 \text{ l m}^{-2} \text{ h}^{-1} \text{ bar}^{-1}$. Therefore, when processing solutions of equal volume, PA-SNFC membranes consumed less than half the energy of traditional NF membranes such as NF 270 ($13.2 \text{ l m}^{-2} \text{ h}^{-1} \text{ bar}^{-1}$) (ref. 38). With increasing SNFC dosage, the rejection of Na_2SO_4 tended to increase, eventually reaching 99.4%. Owing to the enhanced surface charge, a stronger Donnan potential was formed to reject the multivalent SO_4^{2-} . Additionally, the reduced pore size further enhanced the size-sieving effect. When SO_4^{2-} migrates from the high-dielectric constant aqueous solution to the lower-dielectric constant membrane, its large hydration shell and high charge density require greater dehydration energy, making it more easily rejected by the membrane. However, when composed of monovalent Na^+ and Cl^- , NaCl was difficult to reject via the Donnan effect. The increased size-sieving effect resulting from the reduced pore size, which works in synergy with the dielectric effect, led to an increase in NaCl rejection from 7.9% to 10.4%.

Owing to the substantial increase in SO_4^{2-} rejection, the separation coefficient of NaCl and Na_2SO_4 ($\alpha_{\text{Cl}^-/\text{SO}_4^{2-}}$) increased from 9.4 to 144.5, which was markedly superior to that of state-of-the-art PA membranes and various commercial NF membranes (Fig. 4b and Supplementary Fig. 38) and exceeded the upper limit of trade-off.

Assessing the separation performance of various salts (Fig. 4c), the rejection of MgSO_4 and CaSO_4 exhibited a slight decrease in sulfate salts dominated by divalent anions, which is consistent with the typical characteristics of negatively charged membranes. In contrast,

chloride salts were minimally influenced by the Donnan effect and were predominantly controlled by the pore size distribution. Consequently, the rejection of MgCl_2 and CaCl_2 was greater than that of NaCl because of the larger hydration radii of Mg^{2+} and Ca^{2+} . The NF performance of the SNFC/PES composite substrate was also tested, as shown in Supplementary Fig. 39. The rejection of Na_2SO_4 (3.48%) was still greater than that of NaCl (0.17%), indicating that the interlayer can serve as an additional safeguard for the separation of $\text{Cl}^-/\text{SO}_4^{2-}$.

NF performance in practical applications is limited by complex conditions, prompting an investigation of ion sieving under different testing conditions. As presented in Supplementary Fig. 40, an increase in the Na_2SO_4 concentration led to a slight decrease in membrane rejection and permeance, which was attributed to compression of the electrical double layer. The performance remained stable across different operating pressures (Supplementary Fig. 41). In a mixed feed solution of Na_2SO_4 and NaCl, the $\alpha_{\text{Cl}^-/\text{SO}_4^{2-}}$ of the highly ionized membrane increased to 225.5 (Supplementary Fig. 42) owing to the competitive interaction between the ions.

MD simulations were conducted to investigate the sieving mechanism across the PA-SNFC membrane and the transmembrane behaviour under different charge densities. The models (Fig. 4d and Supplementary Fig. 43) were constructed with the left side as the feed side containing SO_4^{2-} and the right side as the permeate side containing the PA layer. After pressure was applied, SO_4^{2-} easily permeated through the membranes in the low charge density model, whereas in the high charge density model, SO_4^{2-} was rejected by the highly ionized PA layer (Supplementary Fig. 44). Furthermore, a smaller D ($0.41 \times 10^{-5} \text{ cm}^2 \text{ s}^{-1}$) was obtained for SO_4^{2-} in the high charge density model than in the low charge density model ($0.88 \times 10^{-5} \text{ cm}^2 \text{ s}^{-1}$) (Fig. 4e). The time dependence of the electrostatic force was inferred from Fig. 4f. According to

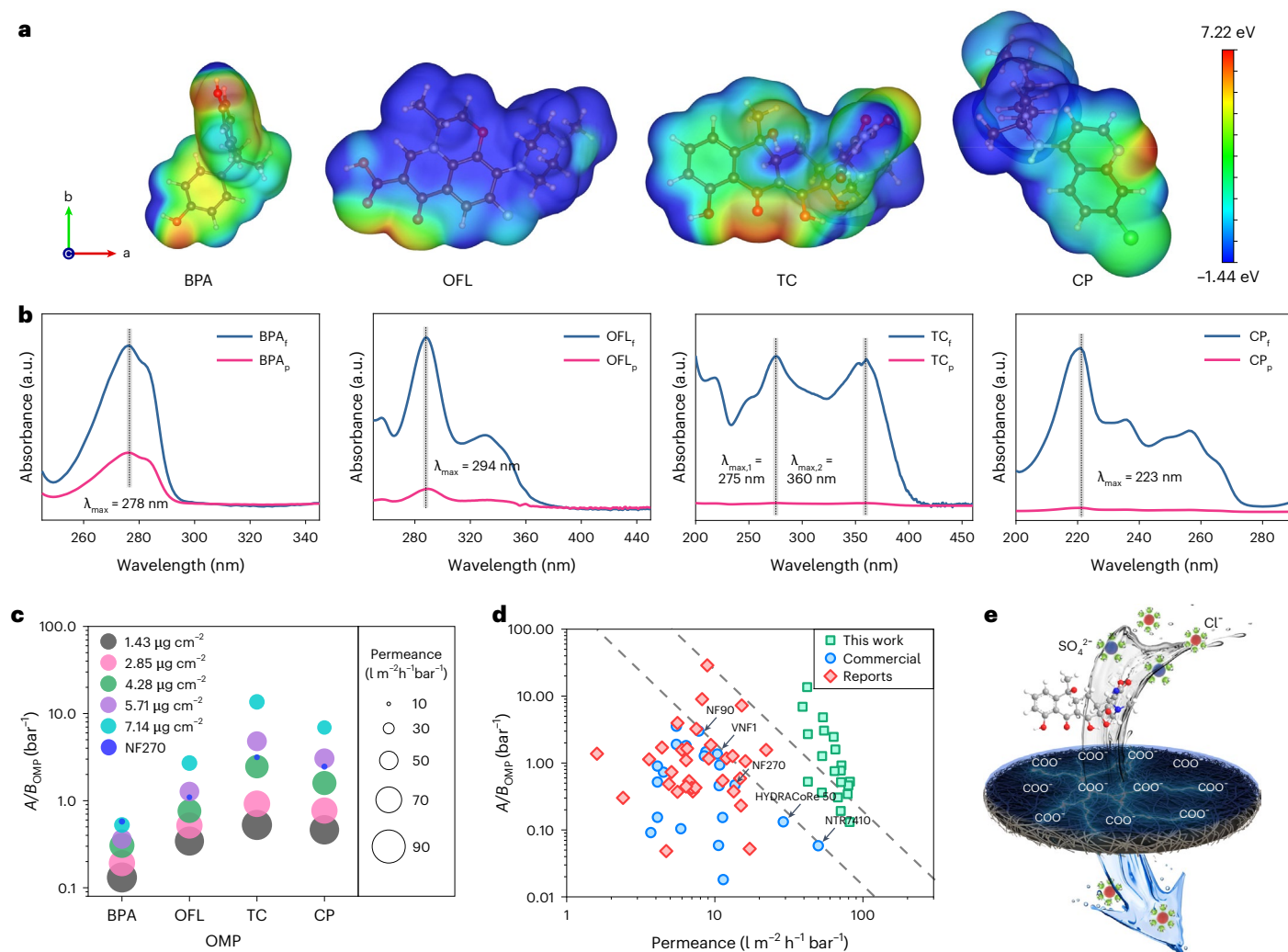


Fig. 5 | Removal of different OMPs. **a**, ESP on the van der Waals surface of BPA (1.22 nm × 0.79 nm × 0.66 nm), OFL (1.57 nm × 1.01 nm × 0.61 nm), TC (1.48 nm × 1.04 nm × 0.91 nm) and CP (1.45 nm × 0.99 nm × 0.85 nm). **b**, Ultraviolet–visible absorption spectra of BPA, OFL, TC and CP in water before (feed) and after (permeate) selectivity tests performed with a PA–SNFC membrane (7.14 $\mu\text{g cm}^{-2}$). **c**, Separation performances of BPA, OFL, TC and CP by PA–SNFC membranes and NF270. The size of the circle represents permeance, the colour of the circle represents different membranes, the horizontal axis

represents different OMPs and the vertical axis represents water/OMP selectivity (A/B_{OMP}). **d**, Trade-off effect between permeance and A/B_{OMP} for PA–SNFC membranes, commercial and state-of-the-art membranes. The traditional upper bound was plotted according to a review⁷. **e**, Schematic diagram of anion sieving and OMP removal by a highly ionized PA–SNFC membrane. The blue balls represent hydrated SO₄²⁻, the red balls represent hydrated Cl⁻ and the organic molecules are negatively charged OMPs represented by TC.

the high charge density model, the Coulomb force between -COOH and SO₄²⁻ was 840.2 kJ mol⁻¹, which is greater than the value of 278.1 kJ mol⁻¹ in the low charge density model. This indicated that SO₄²⁻ faced a greater energy barrier when it crossed the highly ionized PA layer.

Enhanced removal of OMPs

The removal of OMPs, including endocrine disrupting compounds, antibiotics and pharmaceutically active compounds, was investigated via the separation performance of bisphenol A (BPA), ofloxacin (OFL), tetracycline hydrochloride (TC) and chloroquine phosphate (CP). The electrostatic potential (ESP) and physico-chemical properties of the four organics are shown in Fig. 5a and Supplementary Table 7. OFL, TC and CP are electronegative, and their rejection could be enhanced by the negative electrostatic repulsion of the PA–SNFC membrane. For non-negatively charged OMPs such as BPA, the narrower and sharper pore size distribution of the PA–SNFC membrane still contributes to their rejection. In fact, most OMPs in natural waters are negatively charged due to acidic groups such as carboxyl and phenolic functional groups³⁹. In practical applications, positively charged OMPs

may complex with negatively charged OMPs, which are predominant in water, forming larger complexes that can be effectively rejected by the PA–SNFC membrane.

The UV spectra before and after filtration (Fig. 5b) visually revealed the efficient removal of OMPs. As shown in Fig. 5c and Supplementary Figs. 45 and 46, the separation performance of the PA–SNFC membranes was much better than that of NF270, especially in terms of permeance. For neutral BPA, the A/B of the PA–SNFC membrane (7.14 $\mu\text{g cm}^{-2}$) was close to that of NF270, but for negative OFL, TC and CP, the A/B of the PA–SNFC membrane was greater under the promotion of ultra-high charge density. Taking TC as an example, the A/B of the PA–SNFC membranes increased 25.7 times from 0.53 bar^{-1} to 13.6 bar^{-1} , whereas that of NF270 was only 3.15 bar^{-1} . Compared with the MWCO curves of the PA–SNFC membranes calculated with PEG (Fig. 2g), the rejection of BPA was greater than that of PEG with the same molecular weight because BPA has a larger z-axis dimension (nonlinear structure with twisting corners) in the 3D molecular dimension (Supplementary Table 8). Although the molecular weight of CP is greater than that of TC, TC resulted in greater rejection (98.19%) because the 3D molecular

dimension of TC was larger than that of CP. Owing to the increased charge density, OFL resulted in better rejection than BPA despite its smaller z-axis dimension.

Compared with commercial membranes and advanced membranes reported in the literature (Fig. 5d), the PA–SNFC membrane surpasses the upper limit of the trade-off boundary, demonstrating superior OMP separation performance. The stability of the PA–SNFC membrane was confirmed by a 120 h running test. As shown in Supplementary Fig. 47, the rejection and permeance remained stable. Figure 5e shows that the PA NF membranes with ultra-high negative charge density in this work could realize precise anion sieving and removal of OMPs.

Conclusion

In conclusion, we fabricated PA NF membranes with ultra-high negative charge density (-32.6 mC m^{-2}) by controlling the [O] site exposure density. Under the competitive effect among enhanced hydrogen bonding, induction forces, dispersion forces and diffusion driving forces, the diffusion rates of PIP decreased greatly by 73.1%, as confirmed by the use of Einstein's relationships on the basis of the slope of the MSD curve. Tunable monomer diffusion provided varying proportions of PIP and TMC at the interface and formed a uniform incipient thin layer to construct carboxyl-rich PA surfaces ($\text{ratio}_{\text{COO}^-} = 45.7\%$). The highly ionized PA–SNFC membrane possessed a high water permeance of $41.5 \text{ l m}^{-2} \text{ h}^{-1} \text{ bar}^{-1}$, excellent anion selectivity ($\alpha_{\text{Cl}^-/\text{SO}_4^{2-}}$) of 144.5 and notably increased water/OMP selectivity of different OMPs (BPA, OFL, TC and CP). This work provides insights for further improving NF performance and exploring inherent separation mechanisms.

Methods

General

The materials used in this work and the detailed NFCs (BC, WNFC and SNFC) extraction processes are provided in the Supplementary Materials.

Preparation of PA–NFC membranes

The commercial PES microfiltration substrate (diameter: 5 cm, pore size: $0.22 \mu\text{m}$) was presoaked in 50 ml of pure isopropanol for 10 min. Afterward, the membrane was thoroughly rinsed three times with $18.2 \text{ M}\Omega \text{ cm}^{-1}$ ultra-pure water (Milli-Q, Millipore) and transferred to a vacuum filtration apparatus with tweezers. Under 0.1 MPa , 2, 4, 6, 8 and 10 ml of the pre-prepared nanofibrillated cellulose (NFC) solutions ($8.96 \mu\text{g ml}^{-1}$) were filtered on a PES substrate with an effect area of 12.56 cm^2 to obtain NFC dosages of $1.43 \mu\text{g cm}^{-2}$, $2.85 \mu\text{g cm}^{-2}$, $4.28 \mu\text{g cm}^{-2}$, $5.71 \mu\text{g cm}^{-2}$ and $7.14 \mu\text{g cm}^{-2}$, respectively. The membrane was then dried in an oven at $60 \text{ }^\circ\text{C}$ for 10 min to obtain the NFC/PES composite substrate.

The PA–NFC membranes were prepared via an IP reaction on the NFC–PES composite substrate. To prepare the aqueous phase solution with a PIP concentration of 0.05 w/v%, PIP (50 mg), trimethylamine (2 ml) and (\pm)-10-camphorsulfonic acid (1,000 mg) were dissolved in ultra-pure water (100 ml). For the organic phase solution with a TMC concentration of 0.04 w/v%, TMC (40 mg) was dissolved in *n*-hexane (100 ml). The NFC/PES composite substrate was immersed in the water phase (20 ml) for 1 min. The membrane was then allowed to dry in air until no water was noticeably present on the surface. Afterward, the organic phase solution was carefully poured onto the membrane surface and incubated for 1 min. Finally, the PA–NFC membranes were heated at $80 \text{ }^\circ\text{C}$ for 15 min and stored in ultra-pure water before use.

Preparation of PA membranes at the free interface

Two groups of PA membranes formed at the free water/organic interface. In Group A, 10 ml of SNFC/PIP solution and 10 ml of TMC solution were sequentially added to a vacuum filtration apparatus, and after reacting for 1 min, the SNFC in the water phase and the PA layer at the

interface were vacuum filtered onto a PES substrate with a diameter of 4 cm. In Group B, the SNFC/PES substrate was prepared and placed in the filtration apparatus, followed by the sequential addition of 10 ml PIP solution and 10 ml TMC solution (with 10 ml PIP solution serving to isolate SNFC from influencing the IP reaction). After the IP reaction, the PA layer was filtered onto the SNFC/PES substrate. The dosages of the chemicals used were the same as those used for the PA–SNFC membrane (with an SNFC dosage of $7.14 \mu\text{g cm}^{-2}$) mentioned above.

Characterization

SEM images were taken with a Nova Nano SEM 450 (FEI) and AFM images were obtained on a Nanoscope V Multimode 8 scanning probe microscope (Bruker). The thicknesses of the PA layers and SNFC layers were evaluated via cross-sectional transmission electron microscopy (TEM) (JEM-2100Plus, JEOL) and ultra-thin section samples were prepared via EM UC7 (Leica). Powder X-ray diffraction patterns were obtained on a D8 Advance (Bruker). Fourier transform infrared spectroscopy ($4,000\text{--}400 \text{ cm}^{-1}$) was performed using a Nicolet iS20 (Thermo Fisher). The XPS results were obtained via K-alpha X-ray photoelectron spectroscopy (Thermo Fisher). The water contact angle was detected via a contact angle goniometer (JY-82C, Dingsheng). The zeta potential values of the membranes were determined through an electrokinetic analyser (SurPAS 3, Anton Paar). KPFM was performed with a Bruker Dimension Icon instrument (Bruker). The diffusion rate of PIP through the water-oil interface was recorded via UV-vis spectroscopy (U-3010, Hitachi). The concentration of the PEG solution was determined via a total organic carbon analyser (TOC, Elementar). The free volume sizes and distributions of the PA–SNFC membranes were identified via PALS (DPLS3000). Nanoindentation/scratch tests were performed via a NanoTest system (NanoTest, Micro Materials).

Separation performance of ions and OMPs

The membrane performance was assessed via a cross-flow filtration set-up (SF-SA, Saifei), with an effective membrane area of 7.07 cm^2 . Before measurement, the membranes were compacted via ultra-pure water at 6 bar for 1 h. The permeance and rejection of OMPs and salts were analysed via filtration tests, and the effluent was collected at 4 bar after 2 h. The concentrations of OMPs (including BPA, OFL, TC and CP) and salts (including Na_2SO_4 , MgSO_4 , CaSO_4 , MgCl_2 , CaCl_2 and NaCl) in the feed solutions were 10 mg l^{-1} and 1 g l^{-1} , respectively. The concentrations of Na_2SO_4 and NaCl in the mixed salt solutions were both 1 g l^{-1} , and the concentrations of SO_4^{2-} and Cl^- were analysed via ion chromatography (IC, ICS-1100, Thermo Fisher). The measurements were replicated three times, with the results obtained as arithmetic averages.

The solution permeance (A , $\text{l m}^{-2} \text{ h}^{-1} \text{ bar}^{-1}$) was detected via an online weight monitoring system and calculated via equations (1) and (2).

$$\Delta\pi = \Delta cRT \quad (1)$$

$$A = \frac{V}{S \times \Delta t \times (\Delta P - \Delta\pi)} \quad (2)$$

where $\Delta\pi$ (bar) is the osmotic pressure difference across the membrane, Δc (mol l^{-1}) is the solution molarity difference, R ($8.314 \text{ J K}^{-1} \text{ mol}^{-1}$) is the ideal gas constant, T (K) is the absolute temperature, V (l) is the permeate volume, S (m^2) is the effective membrane area, Δt (h) is the sampling interval and ΔP (bar) is the operating pressure.

The solute rejections (R , %), solute permeability coefficient (B , $\text{l m}^{-2} \text{ h}^{-1}$), water/solute selectivity (A/B , bar^{-1}) and $\text{Cl}^-/\text{SO}_4^{2-}$ selectivity ($\alpha_{\text{Cl}^-/\text{SO}_4^{2-}}$) were calculated as follows^{40,41}:

$$R = \left(1 - \frac{C_p}{C_f}\right) \times 100\% \quad (3)$$

$$B = \frac{A(\Delta P - \Delta\pi)(1 - R)}{R} \quad (4)$$

$$\alpha_{\text{Cl}^-/\text{SO}_4^{2-}} = \frac{(C_{\text{Cl}^-}/C_{\text{SO}_4^{2-}})_p}{(C_{\text{Cl}^-}/C_{\text{SO}_4^{2-}})_f} = \frac{1 - R_{\text{Cl}^-}}{1 - R_{\text{SO}_4^{2-}}} \quad (5)$$

where C_p and C_f (g l^{-1}) are the concentrations of the permeate and feed solutions, respectively. The OMP and salt concentrations were quantified via high-performance liquid chromatography (LC-20AT, Shimadzu) and an electrical conductivity meter (FiveEasy FE38, Mettler Toledo).

Calculation of the membrane surface charge density

The Gouy–Chapman equation^{42,43} was used to calculate the membrane charge density (σ , mC m^{-2}), as shown in equations (6) and (7).

$$\kappa^{-1} = \left(\frac{\varepsilon RT}{2F^2 C} \right)^{\frac{1}{2}} \quad (6)$$

$$\sigma = -\varepsilon \kappa \xi \frac{\sinh\left(\frac{F\xi}{2RT}\right)}{\frac{F\xi}{2RT}} \quad (7)$$

where κ^{-1} (m) is the Debye length, ε ($6.933 \times 10^{-10} \text{ F m}^{-1}$) is the permittivity, R ($8.314 \text{ J mol}^{-1} \text{ K}^{-1}$) is the ideal gas constant, T (K) is the absolute temperature, F ($96,485 \text{ C mol}^{-1}$) is the Faraday constant, C (mol m^{-3}) is the concentration of the electrolyte and ξ (V) is the membrane zeta potential tested at pH 7.

Calculation of the free volume of the membrane

The free volume radius (r_i) at the Angstrom scale of the PA layers derived from the annihilation lifetime distribution of ortho-positronium (o-Ps) was calculated via equation (8)⁴⁴.

$$\tau_i = \frac{1}{2} \left[1 - \frac{r_i}{r_i + \Delta r} + \left(\frac{1}{2\pi} \right) \sin\left(\frac{2\pi r_i}{r_i + \Delta r} \right) \right]^{-1} \quad (8)$$

where τ_i is the o-Ps pick-off lifetime and Δr (0.1656 nm) is the thickness of an electron layer that surrounds the free volume spherical potential.

Data availability

The data that support the findings of this study are available upon request.

Code availability

The codes for the MD simulations performed in this study are available upon request.

References

- Elimelech, M. & Phillip, W. A. The future of seawater desalination: energy, technology, and the environment. *Science* **333**, 712–717 (2011).
- Qu, S. et al. Product-to-parent reversion of trenbolone: unrecognized risks for endocrine disruption. *Science* **342**, 347–351 (2013).
- Pehrsson, E. C. et al. Interconnected microbiomes and resistomes in low-income human habitats. *Nature* **533**, 212–216 (2016).
- Wilkinson, J. L. et al. Pharmaceutical pollution of the world's rivers. *Proc. Natl. Acad. Sci. USA* **119**, e2113947119 (2022).
- Tan, Z., Chen, S., Peng, X., Zhang, L. & Gao, C. Polyamide membranes with nanoscale Turing structures for water purification. *Science* **360**, 518–521 (2018).
- Guo, B. B. et al. Double charge flips of polyamide membrane by ionic liquid-decoupled bulk and interfacial diffusion for on-demand nanofiltration. *Nat. Commun.* **15**, 2282 (2024).
- Liu, Y. et al. Boosting the performance of nanofiltration membranes in removing organic micropollutants: trade-off effect, strategy evaluation, and prospective development. *Environ. Sci. Technol.* **56**, 15220–15237 (2022).
- Chowdhury, M. R., Steffes, J., Huey, B. D. & McCutcheon, J. R. 3D printed polyamide membranes for desalination. *Science* **361**, 682–686 (2018).
- Xu, X. et al. Dually charged polyamide nanofiltration membrane incorporated UiO-66-(NH₂)₂: synergistic rejection of divalent cations and anions. *Sep. Purif. Technol.* **311**, 123223 (2023).
- Park, H. B., Kamcev, J., Robeson, L. M., Elimelech, M. & Freeman, B. D. Maximizing the right stuff: the trade-off between membrane permeability and selectivity. *Science* **356**, eaab0530 (2017).
- Liang, Y. et al. Polyamide nanofiltration membrane with highly uniform sub-nanometre pores for sub-1 angstrom precision separation. *Nat. Commun.* **11**, 2015 (2020).
- Sarkar, P., Modak, S. & Karan, S. Ultraselective and highly permeable polyamide nanofilms for ionic and molecular nanofiltration. *Adv. Funct. Mater.* **31**, 2007054 (2021).
- Shen, L. et al. Polyamide-based membranes with structural homogeneity for ultrafast molecular sieving. *Nat. Commun.* **13**, 500 (2022).
- Karan, S., Jiang, Z. W. & Livingston, A. G. Sub-10 nm polyamide nanofilms with ultrafast solvent transport for molecular separation. *Science* **348**, 1347–1351 (2015).
- Chisca, S. et al. Polytriazole membranes with ultrathin tunable selective layer for crude oil fractionation. *Science* **376**, 1105–1110 (2022).
- Jiang, Z., Karan, S. & Livingston, A. G. Water transport through ultrathin polyamide nanofilms used for reverse osmosis. *Adv. Mater.* **30**, 1705973 (2018).
- Wang, Z. et al. Nanoparticle-templated nanofiltration membranes for ultrahigh performance desalination. *Nat. Commun.* **9**, 2004 (2018).
- Wen, Y. et al. Metal-organic framework enables ultraselective polyamide membrane for desalination and water reuse. *Sci. Adv.* **8**, eabm4149 (2022).
- Shao, S. et al. Nanofiltration membranes with crumpled polyamide films: a critical review on mechanisms, performances, and environmental applications. *Environ. Sci. Technol.* **56**, 12811–12827 (2022).
- Zhang, Y. et al. Ice-confined synthesis of highly ionized 3D-quasilayered polyamide nanofiltration membranes. *Science* **382**, 202–206 (2023).
- Zhu, J. et al. Elevated performance of thin film nanocomposite membranes enabled by modified hydrophilic MOFs for nanofiltration. *ACS Appl. Mater. Interfaces* **9**, 1975–1986 (2017).
- Han, S. et al. Microporous organic nanotube assisted design of high performance nanofiltration membranes. *Nat. Commun.* **13**, 7954 (2022).
- Szymczyk, A. & Fievet, P. Investigating transport properties of nanofiltration membranes by means of a steric, electric and dielectric exclusion model. *J. Membr. Sci.* **252**, 77–88 (2005).
- Lu, X. & Elimelech, M. Fabrication of desalination membranes by interfacial polymerization: history, current efforts, and future directions. *Chem. Soc. Rev.* **50**, 6290–6307 (2021).
- Hu, A. et al. Tailoring properties and performance of thin-film composite membranes by salt additives for water treatment: a critical review. *Water Res.* **234**, 119821 (2023).
- Zhu, L. et al. Shapeable fibrous aerogels of metal-organic-frameworks templated with nanocellulose for rapid and large-capacity adsorption. *ACS Nano* **12**, 4462–4468 (2018).

27. Li, S. C. et al. General synthesis and solution processing of metal-organic framework nanofibers. *Adv. Mater.* **34**, 2202504 (2022).
28. Huang, J. et al. Polymeric membranes with highly homogenized nanopores for ultrafast water purification. *Nat. Sustain.* **7**, 901–909 (2024).
29. Yuan, B. et al. Self-assembled dendrimer polyamide nanofilms with enhanced effective pore area for ion separation. *Nat. Commun.* **15**, 471 (2024).
30. Zhang, Y. et al. Insight into the efficient co-removal of Cr(VI) and Cr(III) by positively charged UiO-66-NH₂ decorated ultrafiltration membrane. *Chem. Eng. J.* **404**, 126546 (2021).
31. Zhao, S. et al. Polyamide membranes with tunable surface charge induced by dipole–dipole interaction for selective ion separation. *Environ. Sci. Technol.* **58**, 5174–5185 (2024).
32. Liu, T. et al. Covalent organic framework membrane for efficient removal of emerging trace organic contaminants from water. *Nat. Water* **1**, 1059–1067 (2023).
33. Zuo, P. et al. Near-frictionless ion transport within triazine framework membranes. *Nature* **617**, 299–305 (2023).
34. Bai, Y. et al. Microstructure optimization of bioderived polyester nanofilms for antibiotic desalination via nanofiltration. *Sci. Adv.* **9**, eadg6134 (2023).
35. Wang, K. et al. Tailored design of nanofiltration membranes for water treatment based on synthesis-property-performance relationships. *Chem. Soc. Rev.* **51**, 672–719 (2022).
36. Freger, V. Nanoscale heterogeneity of polyamide membranes formed by interfacial polymerization. *Langmuir* **19**, 4791–4797 (2003).
37. Gan, Q. et al. Nanofoamed polyamide membranes: mechanisms, developments, and environmental implications. *Environ. Sci. Technol.* **58**, 20812–20829 (2024).
38. Cheng, P. et al. Enhancing nanofiltration selectivity of metal-organic framework membranes via a confined interfacial polymerization strategy. *Environ. Sci. Technol.* **57**, 12879–12889 (2023).
39. Levchuk, I., Rueda Marquez, J. J. & Sillanpaa, M. Removal of natural organic matter (NOM) from water by ion exchange—a review. *Chemosphere* **192**, 90–104 (2018).
40. Liu, Y. et al. Efficient capture of endocrine-disrupting compounds by a high-performance nanofiltration membrane for wastewater treatment. *Water Res.* **227**, 119322 (2022).
41. Wang, Z. et al. Nanofiltration membranes with octopus arm-sucker surface morphology: filtration performance and mechanism investigation. *Environ. Sci. Technol.* **55**, 16676–16686 (2021).
42. Zhang, M. et al. Controllable ion transport by surface-charged graphene oxide membrane. *Nat. Commun.* **10**, 1253 (2019).
43. Xu, R., Kang, Y., Zhang, W., Pan, B. & Zhang, X. Two-dimensional MXene membranes with biomimetic sub-nanochannels for enhanced cation sieving. *Nat. Commun.* **14**, 4907 (2023).
44. Si, Z. et al. The ultrafast and continuous fabrication of a polydimethylsiloxane membrane by ultraviolet-induced polymerization. *Angew. Chem. Int. Ed.* **58**, 17175–17179 (2019).
45. Zhao, C. et al. Polyamide membranes with nanoscale ordered structures for fast permeation and highly selective ion-ion separation. *Nat. Commun.* **14**, 1112 (2023).
46. Shen, Q. et al. When self-assembly meets interfacial polymerization. *Sci. Adv.* **9**, ead6122 (2023).
47. Dai, R. et al. Nanovehicle-assisted monomer shuttling enables highly permeable and selective nanofiltration membranes for water purification. *Nat. Water* **1**, 281–290 (2023).

Acknowledgements

This work was supported by the National Natural Science Foundation of China (number 52470080, F.L.) and the Major Science and Technology Program for Water Pollution Control and Treatment of China (number 2014ZX07204-008, F.L.). X.X. acknowledges the China Scholarship Council for funding a scholarship (CSC, number 202306190105) and Monash University for hosting her visiting research. The bacterial cellulose was kindly provided by Hainan Guangyu Biotechnology Co. We gratefully acknowledge W. Jin's group at Nanjing Tech University for assistance with nanoindentation/scratch tests.

Author contributions

F.L. and H.W. conceived the idea and designed the experiments. X.X., Y.C., Z.W. and G.H. carried out the material synthesis, characterization and performance tests. Z.Z. and S.L. performed the MD simulations. X.X. and P.J. performed the data analysis. All coauthors discussed the results. X.X. wrote the manuscript. P.J., F.L. and H.W. revised the manuscript.

Funding

Open access funding provided by Monash University

Competing interests

The authors declare no competing interests.

Additional information

Supplementary information The online version contains supplementary material available at <https://doi.org/10.1038/s44221-025-00440-9>.

Correspondence and requests for materials should be addressed to Fuqiang Liu or Huanting Wang.

Peer review information *Nature Water* thanks the anonymous reviewers for their contribution to the peer review of this work.

Reprints and permissions information is available at www.nature.com/reprints.

Publisher's note Springer Nature remains neutral with regard to jurisdictional claims in published maps and institutional affiliations.

Open Access This article is licensed under a Creative Commons Attribution 4.0 International License, which permits use, sharing, adaptation, distribution and reproduction in any medium or format, as long as you give appropriate credit to the original author(s) and the source, provide a link to the Creative Commons licence, and indicate if changes were made. The images or other third party material in this article are included in the article's Creative Commons licence, unless indicated otherwise in a credit line to the material. If material is not included in the article's Creative Commons licence and your intended use is not permitted by statutory regulation or exceeds the permitted use, you will need to obtain permission directly from the copyright holder. To view a copy of this licence, visit <http://creativecommons.org/licenses/by/4.0/>.

© The Author(s) 2025